ANNUAL REVIEWS

Annual Review of Fluid Mechanics

Drop Impact Dynamics: Impact Force and Stress Distributions

Xiang Cheng,[1] Ting-Pi Sun,[1] and Leonardo Gordillo[2]

[1]Department of Chemical Engineering and Materials Science, University of Minnesota, Minneapolis, Minnesota, USA; email: xcheng@umn.edu

[2]Departamento de Física, Facultad de Ciencia, Universidad de Santiago de Chile (USACH), Santiago, Chile

Annu. Rev. Fluid Mech. 2022. 54:57–81

First published as a Review in Advance on September 23, 2021

The *Annual Review of Fluid Mechanics* is online at fluid.annualreviews.org

https://doi.org/10.1146/annurev-fluid-030321-103941

Keywords

impact force, pressure, shear stress, self-similarity, singularity, boundary layer, air cushioning, erosion

Abstract

Dynamic variables of drop impact such as force, drag, pressure, and stress distributions are key to understanding a wide range of natural and industrial processes. While the study of drop impact kinematics has been in constant progress for decades thanks to high-speed photography and computational fluid dynamics, research on drop impact dynamics has only peaked in the last 10 years. Here, we review how recent coordinated efforts of experiments, simulations, and theories have led to new insights on drop impact dynamics. Particularly, we consider the temporal evolution of the impact force in the early- and late-impact regimes, as well as spatiotemporal features of the pressure and shear-stress distributions on solid surfaces. We also discuss other factors, including the presence of water layers, air cushioning, and nonspherical drop geometry, and briefly review granular impact cratering by liquid drops as an example demonstrating the distinct consequences of the stress distributions of drop impact.

1. INTRODUCTION

Drop impact is so familiar to us that we are usually indifferent to this elegant ephemeral fluid process in our daily life, for example, when raindrops fall on our skin with small yet perceptible force. However, this everyday phenomenon is of great importance to many natural and industrial processes, ranging from soil erosion (Terry 1998, Planchon & Mouche 2010, Bako et al. 2016) to the dispersion and spreading of airborne pathogens (Joung & Buie 2015, Bourouiba 2021) and the coating and printing of functional materials (Wijshoff 2018). Driven by its ubiquitous presence and vast industrial applications, drop impact has become one of the most extensively studied topics in fluid mechanics.

Although the study of drop impact can be traced back nearly 150 years to the pioneering work of Worthington (1876), significant progress has only been made in the past three decades thanks to the fast development of high-speed photography techniques (Josserand & Thoroddsen 2016). In combination with advanced numerical algorithms enabled by increasing computational power (Scardovelli & Zaleski 1999, Popinet 2009), researchers can now elucidate the spatiotemporal structures of fast drop impact events with unprecedented detail. A wide range of theoretical concepts including Wagner's (1932) impact theory, viscous boundary layers (Schlichting & Gersten 2000), self-similarity (Barenblatt 1996), and finite-time singularity (Eggers 1997, Eggers & Fontelos 2015) have been invoked and integrated to decipher the dynamics of drop impact.

Nevertheless, relying upon direct imaging, most experiments have focused on the kinematics of impact processes, i.e., the morphological changes of impacting drops (**Figure 1**). Kinematic features such as the maximum spreading diameter (Bennett & Poulikakos 1993, Clanet et al. 2004, Ukiwe & Kwok 2005, Roisman 2009, Eggers et al. 2010, Laan et al. 2014, Wildeman et al. 2016), the contact time (Richard et al. 2002, Bird et al. 2013), and the splashing threshold (Mundo et al. 1995, Yarin & Weiss 1995, Josserand & Zaleski 2003, Xu et al. 2005, Roisman 2009, Riboux & Gordillo 2014, Howland et al. 2016) have taken the center stage and dominated the study of drop impact. In comparison, relatively fewer studies have been devoted to dynamic properties such as the impact force and stress distributions of drop impact, even though these dynamic variables arguably lead to the most consequential outcomes of drop impact events.

Many early studies of drop impact were motivated by the process of soil erosion (Laws 1940, Ellison 1945, Palmer 1965, Ghadiri & Payne 1977, Imeson et al. 1981, Nearing et al. 1986, Nearing & Bradford 1987), where the impact force and stress distributions of raindrops play a key role in breaking soil aggregates and detaching and transporting granular particles (**Figure 1*b***). Wear and

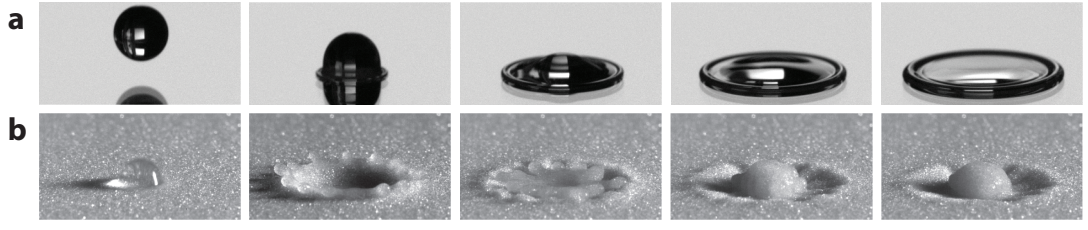

Figure 1

Drop impact kinematics. (*a*) A 3-mm-diameter drop of aqueous glycerol solution with a viscosity of 6 mPa·s and an impact velocity of 1.5 m/s impacts on a glass surface. Frames are 75 μs apart. Panel *a* courtesy of Michelle Driscoll. (*b*) A 3-mm-diameter water drop with an impact velocity of 2.7 m/s impacts on a granular medium made of 90-μm-diameter glass beads. The times of the snapshots are $t = 0.3$ ms, 5.7 ms, 11.9 ms, 19.4 ms, and 56.8 ms after the impact at $t = 0$. Panel *b* adapted with permission from R. Zhao et al. (2015).

damage induced by repeated impact of high-speed drops on solid surfaces such as turbine blades also crucially depend on impact force and stress distributions (Hancox & Brunton 1966, Zhou et al. 2008, Obreschkow et al. 2011, Takekura et al. 2018). Moreover, these dynamic quantities are also the leading factor affecting surface cleaning and jet peening and cutting (Kondo & Ando 2019, Mitchell et al. 2019a). The temporal variation of impact force and stresses also controls the splashing of droplets on soft substrates (Pepper et al. 2008, Howland et al. 2016), as well as the signature of raindrop noises (Prosperetti & Oguz 1993, Yu & Hopkins 2018, Schmid et at. 2021). Lastly, the survival of living organisms exposed to the elements in events such as the collision of flying insects with falling raindrops (Dickerson et al. 2012, Kim et al. 2020) and the abscission of plant leaves by raindrops (Gart et al. 2015) also relies on the transient force impulse of drop impact.

Mach number: $M = V/c$

More fundamentally, impact force and stress distributions can reveal certain aspects of drop impact dynamics, which are hard, if not impossible, to probe from kinematics measurements. Particularly, these dynamic quantities exhibit strong temporal variations at the early time of drop impact, where impacting drops barely deviate from their original spherical shape (Rioboo et al. 2002, Lagubeau et al. 2012, Philippi et al. 2016). Thus, measuring the temporal evolution of the impact force and pressure distribution of drop impact provides a more sensitive way to investigate impact dynamics at early times (Eggers et al. 2010, Philippi et al. 2016). Similarly, the shear stress distribution of drop impact reveals the development of the viscous boundary layer within impacting drops (Roisman 2009, Eggers et al. 2010, Lastakowski et al. 2014, Philippi et al. 2016, Riboux & Gordillo 2017, Gordillo et al. 2019), which is difficult to access by other experimental methods.

There are many excellent reviews focusing on the kinematics of drop impact (Rein 1993, Yarin 2006, Marengo et al. 2011, Josserand & Thoroddsen 2016, Yarin et al. 2017). Instead, we provide here a brief account of the current understanding of the impact force and stress distributions of drop impact. We limit our review on drop impact to moderate impact velocities, where impacting drops can be considered incompressible. The compressibility of impacting drops leads to the so-called water-hammer pressure on the order of ρVc over a time duration of RV/c^2 (Lesser & Field 1983, Nearing et al. 1986, Field et al. 2012). Here, ρ is the density of liquid, V is the impact velocity, c is the speed of sound in the drop, and R is the radius of the drop. For a typical millimeter-sized raindrop impacting at its terminal velocity of ∼10 m/s, ρVc is large, ∼10 MPa. However, the time duration associated with the propagation of the compression wave in the impacting drop is only ∼10 ns. The radius of the contact area over this time interval is on the order of $RV/c \sim 10$ μm. Hence, compressibility affects only the very early moment of impact over a tiny contact area, which is not directly relevant to drop dynamics at long times and is hard to detect experimentally (Soto et al. 2014, Visser et al. 2015, Bako et al. 2016). The effect of air cushioning further screens the water-hammer pressure, as we discuss below. As a result, compressibility is important only for drop impact of very high speeds with the Mach number on the order of one (Lesser & Field 1983), a regime beyond the scope of the current review.

We organize the review as follows. In Section 2, we first consider the temporal evolution of impact force. Experimental and theoretical understanding of drop impact force are discussed in the early-impact regime and the late spreading regime, respectively. We then discuss the pressure and shear stress distributions underneath impacting drops in Section 3. The discussion is limited to spherical drops impacting on a dry smooth solid surface first. Other relevant factors such as the presence of liquid layers, the effect of air cushioning, and nonspherical drop shapes are considered in Section 4. Lastly, we briefly discuss granular impact cratering by liquid drops in Section 5, which provides a concrete example demonstrating the unique role of the stress distributions of drop impact in surface erosion. Open questions and future directions are stated at the end.

2. IMPACT FORCE

2.1. Temporal Evolution of Impact Force

Reynolds number: $Re = DV/\nu$

Weber number: $We = \rho DV^2/\gamma$

Froude number: $Fr = V/\sqrt{gD}$

Impact force is the most studied dynamic quantity of drop impact. Piezoelectric sensors are frequently used for measuring the temporal evolution of the normal force of impacting drops (Imeson et al. 1981; Nearing et al. 1986; Nearing & Bradford 1987; Grinspan & Gnanamoorthy 2010; Li et al. 2014; Soto et al. 2014; Zhang et al. 2017, 2019; Gordillo et al. 2018; Mitchell et al. 2019b; Schmid et at. 2021). Other methods such as cantilever beams (Mangili et al. 2012, Soto et al. 2014, Gart et al. 2015, Chen et al. 2019) and accelerometer arrays attached to elastic plates (Yu & Hopkins 2018) have also been employed for impact force measurements. These measurements are often synchronized with high-speed photography for simultaneous imaging of the morphology of impacting drops (Zhang et al. 2017, 2019; Gordillo et al. 2018; Mitchell et al. 2019b; Schmid et at. 2021).

Figure 2 shows an example of a simultaneous measurement of the shape and of the impact force of a silicone oil drop impacting on the smooth metal surface of a piezoelectric sensor. Upon impact, the contact line of the drop increases immediately following a square-root temporal scaling. Nevertheless, the top of the drop still falls linearly with the original impact velocity at early times, as if the impact had not yet occurred at the bottom. In contrast, the impact force rises quickly upon impact and reaches a maximum when the boundary of the drop is approximately vertical to the impacted surface. The force then decays over much longer times as the drop spreads out radially along the surface. The resulting force–time curve is asymmetric with respect to the peak force. As a comparison, the impact force of an elastic sphere on a flat surface is symmetric, preserving the time-reversal symmetry.

The key dimensionless numbers governing the dynamics of drop impact are the Reynolds number Re and the Weber number We, which compare the inertia of impacting drops with the viscous and capillary forces, respectively. We consider impact conditions with the Froude number $Fr \gg 1$ such that the effect of gravity is negligible. For raindrops impacting at their terminal velocities, we have $Re \sim 10^4$, $We \sim 10^2$–10^3, and $Fr \sim 50$. In the limit of high Re and We, where inertia dominates the impact process, Soto et al. (2014) experimentally demonstrated that the peak force follows the inertial force scaling, $F_{\max} \sim \rho D^2 V^2$. Later experiments by Zhang et al. (2017) further showed that the temporal evolution of the dimensionless impact force $\tilde{F}(\tilde{t})$ exhibits a universal form in this limit, independent of Re and We. Here, the impact force $F(t)$ is nondimensionalized by the inertial force, $\tilde{F} = F/(\rho D^2 V^2)$, and the time is nondimensionalized by the impact time, $\tilde{t} = t/(D/V)$. The universal form has also been confirmed by several independent experiments (**Figure 3*a***) (Gordillo et al. 2018, Yu & Hopkins 2018, Mitchell et al. 2019b). In this review, the dimensionless quantities are represented by adding a tilde on the top of the corresponding dimensional quantities. The time- and length scales used for nondimensionalization are the drop diameter D and impact time D/V, respectively. Pressure is nondimensionalized by ρV^2.

The shape of the universal form is characterized by three features: (*a*) the dimensionless peak force, $\tilde{F}_{\max} = 0.85 \pm 0.05$; (*b*) the dimensionless time when the peak force occurs, $\tilde{t}_{\max} = 0.17 \pm 0.02$; and (*c*) the area underneath the force–time curve before the peak force, which is about one quarter of the total area (**Figure 3*b***) (Gordillo et al. 2018). Note that the total area underneath a force–time curve gives the impulse of the impact event, which is equal to the initial momentum of the impacting drop. Thus, one quarter of the initial momentum has been transferred from the drop to the impacted surface when the peak force is reached.

The deviation from the universal form has been observed under the following conditions. (*a*) When Re is below 200, $\tilde{F}_{\max}$ increases and $\tilde{t}_{\max}$ decreases with decreasing Re (**Figure 3*a***) (Zhang et al. 2017, Gordillo et al. 2018). Although the temporal evolution of the impact force does not

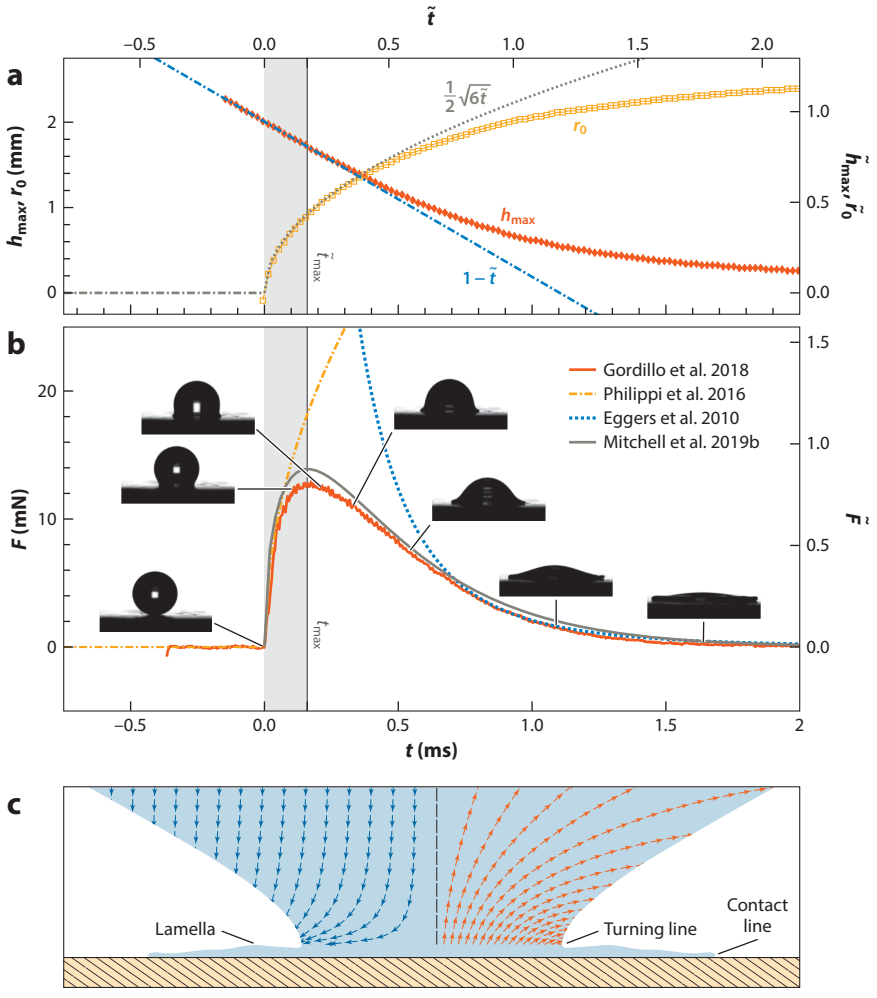

Figure 2

Simultaneous measurements on the kinematics and dynamics of an impacting drop of diameter $D = 2.2$ mm with impact velocity $V = 1.93$ m/s, viscosity $\nu = 20$ cSt, and surface tension $\gamma = 18.9$ mN/m. (*a*) Drop height $h_{max}(t)$ and the radius of the turning line $r_0(t)$. The fitting lines indicate the free fall of h_{max} with V and the scaling of $\tilde{r}_0 = \sqrt{6\tilde{t}}/2$. Here, the dimensionless variables are represented by adding a tilde on the top of the corresponding dimensional variables. The length and time are nondimensionalized by the drop diameter D and the impact time D/V, respectively. The impact force is nondimensionalized by $\rho D^2 V^2$. (*b*) Normal impact force $F(t)$. Experimental results are from Gordillo et al. (2018). Theoretically, Philippi et al. (2016) predicted the impact force in the early-impact regime, whereas the force in the late spreading regime can be derived from the pressure formula of Eggers et al. (2010). Mitchell et al. (2019b) provided an empirical relation covering the entire time domain. Panels *a* and *b* adapted with permission from Gordillo et al. (2018). (*c*) The definition of the turning line at $r_0(t)$. Arrows indicate the flow inside an impacting drop in the lab frame (*left*) and in the reference frame moving with the drop initial impact velocity (*right*).

follow the universal form at low *Re*, the shape of the force-time curves is still invariant. The area underneath the force curve before the peak remains at 1/4 of the total impulse (Gordillo et al. 2018). A good collapse can still be achieved when $F(t)$ is normalized by F_{max} and t is normalized by t_{max} (inset in **Figure 3*a***). (*b*) For large drops near their terminal velocities, $\tilde{F}(\tilde{t})$ also deviates

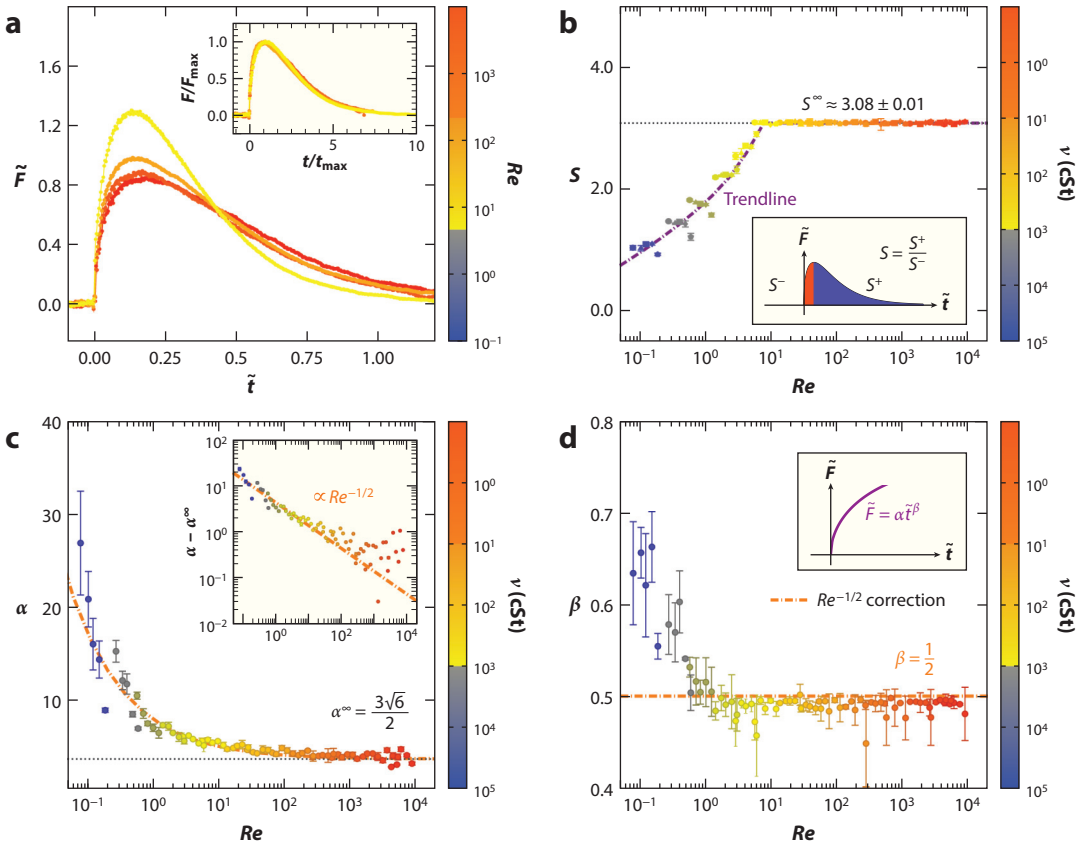

Figure 3

Temporal evolution of impact force. (*a*) Dimensionless impact force, $\tilde{F} = F/(\rho D^2 V^2)$, versus dimensionless time, $\tilde{t} = t/(D/V)$, at different Reynolds numbers, *Re*, where *D* is the drop diameter and *V* is the impact velocity. (*Inset*) Impact force normalized by the peak force F_{max} versus time normalized by the peak time t_{max}. (*b*) The ratio of the area underneath the $F - t$ curves after the peak to that before the peak, *S*, at different *Re*. The inset shows the definition of the area ratio, *S*. (*c*) The numerical prefactor α and (*d*) the scaling exponent β of the impact force $\tilde{F} = \alpha \tilde{t}^{\beta}$ near $t \to 0^+$ (see the *inset* in panel *d*). The inset in panel *c* shows α in a log-log plot. ν is the kinematic viscosity of the drop. Dashed lines are the theoretical prediction (Equation 2). Figure adapted with permission from Gordillo et al. (2018).

from the universal form (Yu & Hopkins 2018). It has been suggested that the deviation arises due to the deformation of large drops under air drag (see Section 4.3). (*c*) The impact force of viscoelastic drops also deviates from the universal form (see **Figures 3*d*** and **4*c*** and discussion below).

The temporal evolution of the impact force naturally divides an impact event into two regimes, i.e., the early-impact regime before the peak force and the later-impact regime after the peak force. Below we consider the dynamics of the impact force in each of these two regimes, separately.

2.2. Early-Impact Regime: Turning Line–Controlled Self-Similar Flow

The early moment of drop impact is driven by inertia and controlled by the sudden change of the direction of flow velocity from downward vertical to outward radial. Such a drastic change occurs over a localized region near the turning line. In the reference frame moving with the drop's initial

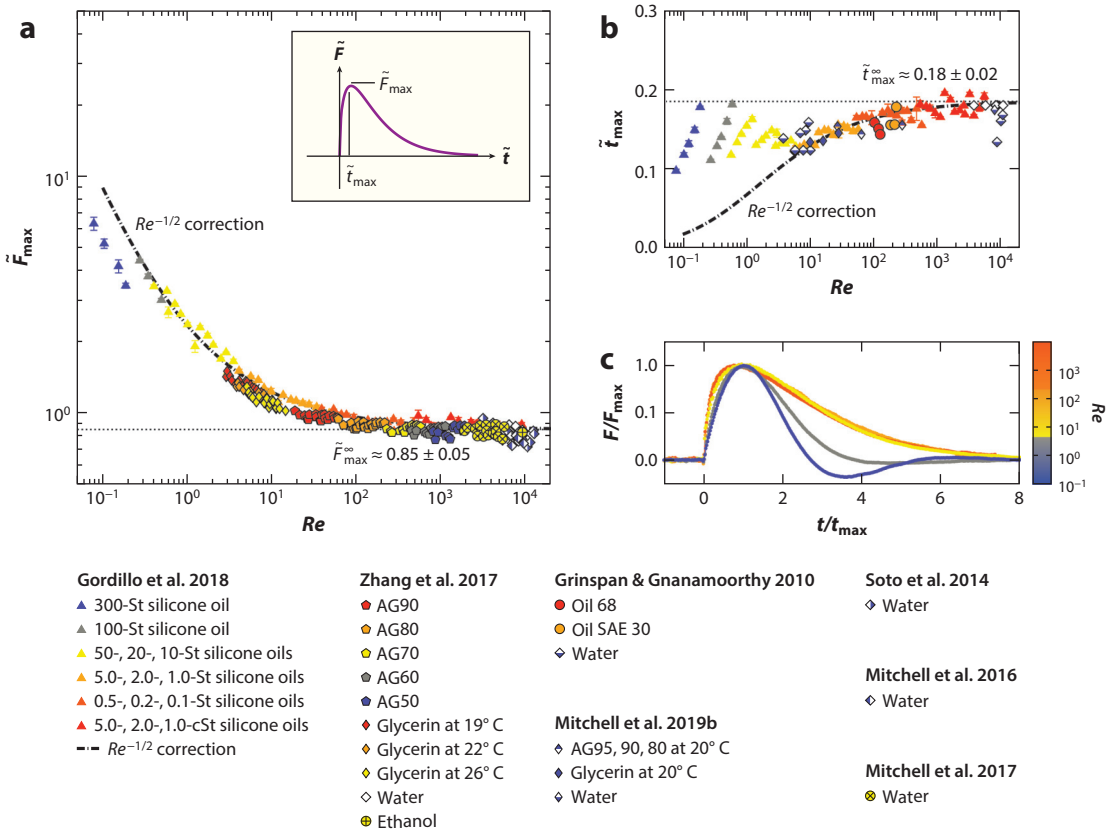

Figure 4

(*a*) Peak force $\tilde{F}_{max}$ (see *inset*) as a function of Reynolds number *Re*. Symbols are from experiments, and the dashed line is the theoretical prediction (Equation 4). (*b*) Peak time $\tilde{t}_{max}$ as a function of *Re*. Symbols are from experiments, and the dashed line is the theoretical prediction (Equation 3). (*c*) Comparison of the force–time curves of viscoelastic drops at low $Re < 7$ with those of Newtonian drops at high *Re*. The color map is the same as that in **Figure 3*a***. Abbreviation: AG*X*, aqueous glycerin of weight percentage *X*%.

impact velocity, the flow inside the drop winds around the turning line, showing a tank-treading movement (**Figure 2*c***). Before the formation of the liquid lamella, the turning line is coincident with the contact line (Philippi et al. 2016). The two terms are used interchangeably. With the liquid lamella, however, the turning line sits at the root of liquid lamella and separates from the contact line at the tip of the lamella. The turning line becomes the waistline of the impacting drop.

Quantitatively, the radius of the turning line follows a square-root scaling, $r_0(t) \sim \sqrt{DVt}$, at high *Re* and *We* near $t \to 0^+$, which was first proposed by Wagner (1932) in the context of the water entry of solid objects. The scaling can be obtained geometrically by considering the intersection of a free-falling drop with the impacted surface at small *t*. Experiments and detailed calculations have confirmed the scaling with a numerical prefactor slightly larger than the simple geometric consideration, $r_0(t) = \sqrt{6DVt}/2$ (**Figure 2*a***) (Riboux & Gordillo 2014, Philippi et al. 2016, Gordillo et al. 2018). Experiments have shown that the peak force is reached when the side wall of the impacting drop is normal to the impacted surface (Mitchell et al. 2019b). The observation suggests $r_0(t = t_{max}) = D/2$ at the peak time, which gives $\tilde{t}_{max} = 1/6$, agreeing with the experimental findings.

The fast horizontal flow on the substrate generates a viscous boundary layer that propagates radially and moves upward. When the length scale of the impact process under consideration l is larger than the thickness of the viscous boundary layer l_v but much smaller than the drop size D, the inertia-driven potential flow should have a self-similar structure with the self-similar variable defined via l/r_0. The condition of self-similarity is satisfied at the early times of high-Re drop impact, as $\tilde{l}_v \approx \sqrt{\tilde{t}/Re} \ll \tilde{r}_0 = \sqrt{6\tilde{t}}/2 \ll 1$ at small $\tilde{t}$. Josserand & Zaleski (2003) first applied the self-similar hypothesis for drop impact on a thin fluid film at early times. They showed that $p = \rho V^{3/2} D^{1/2} t^{-1/2} g(X, Y)$, where $X = 1 - r/r_0$ and $Y = z/r_0$ are the self-similar coordinates and g is a dimensionless scaling function. The impact force then follows as $F \sim p r_0^2 \sim \rho V^{5/2} D^{3/2} t^{1/2}$ or $\tilde{F} \sim \tilde{t}^{1/2}$ in the dimensionless form. Using the length scale set by the turning line r_0, we can also form a simple scaling argument for the impact force. The portion of an impacting drop that decelerates from V to 0 over a time interval of $\mathrm{d}t$ is $\mathrm{d}[r_0^3(t)] \sim (VD)^{3/2} t^{1/2} \mathrm{d}t$, which leads to the change of the axial momentum $\mathrm{d}M \sim \rho V^{5/2} D^{3/2} t^{1/2} \mathrm{d}t$. Thus, the impact force scales as $F = \mathrm{d}M/\mathrm{d}t \sim \rho V^{5/2} D^{3/2} t^{1/2}$.

Philippi et al. (2016) analyzed the detailed structure of the self-similar potential flow for drop impact on a dry surface and obtained an analytical solution for the impact force in the high Re limit as $t \to 0^+$ with an order-one numerical prefactor:

$$\tilde{F} = \frac{3\sqrt{6}}{2} \tilde{t}^{1/2}. \qquad 1.$$

Gordillo et al. (2018) experimentally verified the predicted square-root temporal scaling of the impact force. **Figure 3*c,d*** show the numerical prefactor α and the power exponent β of the temporal scaling of the impact force, extracted from the power law fitting of the experimental force–time curves at early times. Above $Re > 200$, $\alpha = 3\sqrt{6}/2$ and $\beta = 1/2$ quantitatively agree with Equation 1. The square-root scaling has also been confirmed by two other recent experiments and simulations (Mitchell et al. 2019b, Zhang et al. 2019).

At $7 < Re < 200$, the impact force still follows the square-root temporal scaling. However, the numerical prefactor increases with decreasing Re, deviating from the theoretical prediction (**Figure 3*c,d***). To understand the behavior of the impact force at finite Re, Gordillo et al. (2018) performed an asymptotic perturbation calculation by matching the inner velocity profile within a viscous boundary layer and the outer velocity profile in the self-similar potential flow to the first order of $Re^{-1/2}$. They showed that the viscous boundary layer enhances the propagation speed of the self-similar pressure field within the impacting drop, leading to an increased impact force:

$$\tilde{F} = \frac{3\sqrt{6}}{2} \left(1 + \frac{8\sqrt{6}}{3\pi^{3/2}} \frac{1}{Re^{1/2}} \right) \tilde{t}^{1/2}. \qquad 2.$$

Equation 2 quantitatively agrees with experiments without fitting parameters (**Figure 3*c,d***). Note that the viscous boundary layer grows as $l_v \sim \sqrt{\nu t}$, showing the same temporal scaling as $r_0(t)$. Thus, the viscous effect is added as a self-similar correction to the original solution of the potential flow, resulting in the same square-root temporal scaling for the impact force at finite Re. At even lower $Re < 7$, experiments using high–molecular weight silicone oils with viscosity above 1,000 cSt showed an increase of the exponent of the temporal scaling above 1/2 (**Figure 3*d***). In addition, the area of the force–time curves before the peak sharply increases above 1/4 of the total area (**Figure 3*b***) toward the value of 1/2, which is the expected result for the impact of elastic spheres. These qualitative changes are thus attributed to the effect of the viscoelasticity of high–molecular weight silicone oils (Gordillo et al. 2018).

The peak time $\tilde{t}_{\max}$ can be estimated as the time when the self-similar pressure field propagates through the entire impacting drop and terminates the early-time self-similar flow structure. While

the top of an impacting drop decreases linearly with the initial impact velocity following $(D - Vt)$ in the early-impact regime (**Figure 2*a***), the self-similar pressure field propagates upward following $(VD^3t)^{1/4}$ at high Re (Gordillo et al. 2018). The two fronts meet at t_{max} when $(D - Vt_{max}) = A(VD^3t_{max})^{1/4}$, where an order-one geometric factor A is added to count the mismatch of the shape of the isobars and the free surface of the drop. From $\tilde{t}_{max} = 0.17$ at high Re, we have $A = 1.29$. The above argument can be extended to finite-Re impact by considering the enhanced pressure propagation induced by the viscous boundary layer. The dimensionless peak time is given by the solution of the following polynomial equation,

$$(1 - \tilde{t}_{max})^4 - A^4 \left(1 + \tilde{U} Re^{-1/2}\right)^2 \tilde{t}_{max} = 0, \qquad 3.$$

where $\tilde{U} = 8\sqrt{6}/(3\pi^{3/2})$ is the first-order correction to the axial velocity of the outer potential flow. The calculation provides a quantitative prediction of the peak time as a function of Re (**Figure 4*b***) with no fitting parameter. Since the shape of the force–time curves is invariant (inset in **Figure 3*a***), the peak force at low Re can thus be estimated as

$$\tilde{F}_{max}(Re) = \tilde{F}^{\infty}_{max} \frac{\tilde{t}^{\infty}_{max}}{\tilde{t}_{max}(Re)}, \qquad 4.$$

where $\tilde{F}^{\infty}_{max} = 0.85 \pm 0.05$ and $\tilde{t}^{\infty}_{max} = 0.17 \pm 0.02$ are the peak force and time in the high-Re limit, respectively. The equation provides a good estimate of the peak force of viscous drops (**Figure 4*a***). At low $Re < 7$, the prediction deviates from experiments likely because of the viscoelasticity of silicone oils used in experiments. The force–time curves of viscoelastic drops become more symmetric, approaching the behavior of solid-sphere impact (**Figures 3*b*** and **4*c***). Negative forces can also be observed due to the bouncing of the viscoelastic drops on the force sensor (**Figure 4*c***).

2.3. Late-Impact Regime: Drop Spreading

Pressure gradients dominate the impact process in the early-impact regime and redirect the flow from the axial direction to the radial direction. In contrast, the spreading of drop in the late-impact regime is driven by drop inertia in the radial direction. Pressure gradients are insignificant and play only a minor role in the process. Depending on Re and We, the spreading is eventually checked by either viscous forces, capillary forces, or both, giving rise to the maximum spreading diameter (Laan et al. 2014). Nevertheless, from the perspective of impact force, the axial momentum of impacting drops approaches zero near the maximum spreading diameter, which leads to only very weak impact force. Thus, our discussion of the impact force in the late-impact regime focuses on inertia-driven spreading when the force signal is still strong and ignores viscous and capillary effects important toward the end of drop spreading.

Inertia-driven drop spreading is governed asymptotically by a hyperbolic flow (Yarin & Weiss 1995, Fedorchenko et al. 2005, Roisman 2009, Roisman et al. 2009, Eggers et al. 2010): $v_r = r/(t + t_0)$ and $v_z = -2z/(t + t_0)$, where v_r and v_z are the flow velocity in the radial and axial directions, respectively. The term t_0 indicates the onset time of inertia-driven spreading after impact. The associated pressure field can then be obtained from the Euler equations, $p(r, z, t) = 3\rho[h^2(r, t) - z^2]/(t + t_0)^2$, where $h(r, t)$ is the free surface of the spreading drop, which can be further written as $h(r, t) = h_{max}(t)G(\xi)$, where $h_{max} = A_1 D^3/[V(t + t_0)]^2$ is the maximum drop height at $r = 0$ with a fitting constant A_1 and $G(\xi)$ is a dimensionless scaling function (Roisman et al. 2009, Eggers et al. 2010). The variable $\xi = r\sqrt{h_{max}/V_0}$ is a self-similar variable governing drop spreading, and $V_0 = \pi D^3/6$ is the drop volume. The impact force can thus be calculated as

$$\tilde{F}(\tilde{t}) = 2\pi \int_0^{\infty} \tilde{p}(\tilde{r}, \tilde{z} = 0, \tilde{t})\tilde{r}\, d\tilde{r} = \frac{\pi^2 A_1}{(\tilde{t} + \tilde{t}_0)^4} \int_0^{\infty} G^2(\xi)\xi\, d\xi, \qquad 5.$$

which shows a 1/4 power law decay at long times. From experiments on the shape of spreading drops, we obtain $A_1 = 0.492$, $\tilde{t}_0 = 0.429$, and $\int_0^\infty G^2(\xi)\xi \, d\xi = 0.0911$ (Lagubeau et al. 2012). Equation 5 agrees with experiments for $\tilde{t} > 0.8$ (the Eggers et al. line in **Figure 2*b***).

Instead of the power law decay, Mitchell et al. (2019b) showed empirically that the decrease of the impact force can be approximated by an exponential decay:

$$\tilde{F}(\tilde{t}) = \tilde{F}_0 \exp\left(-\frac{\tilde{t} - \tilde{t}_0}{k}\right). \quad 6.$$

From direct fitting, we have $1/k = -2.84$. The exponential decay starts around $\tilde{t}_0 = 0.5$, with $\tilde{F}_0 = 0.53$.

By interpolating the square-root scaling of the early-impact regime and the empirical exponential decay of the spreading regime, Mitchell et al. (2019b) also proposed a simple formula that quantitatively describes the temporal evolution of the impact force over the entire time domain (the Mitchell et al. line in **Figure 2*b***),

$$\tilde{F}(\tilde{t}) = \sqrt{C_1 \tilde{t}} \exp(-C_2 \tilde{t}), \quad 7.$$

where the coefficients $C_1 = 1{,}000\pi/243$ and $C_2 = 10/3$ are fixed by the initial momentum of impacting drops $\rho V_0 V$ and the peak time $\tilde{t}_{\max} = 0.15$. Note that $\sqrt{C_1} \approx 3.60$ is close to the numerical factor $3\sqrt{6}/2 \approx 3.67$. Thus, Equation 7 is asymptotic to Equation 1 in the limit $t \to 0^+$.

3. STRESS DISTRIBUTIONS

3.1. Pressure

Impact force quantifies the average impact pressure but cannot reveal the pressure distribution underneath impacting drops. Indeed, the pressure distribution of an impacting drop is far from uniform, which provides more detailed and interesting information on the dynamics of drop impact. We again divide our discussion into the early- and late-impact regimes.

3.1.1. Early-impact regime. The self-similar scaling in the early-impact regime has shown that $p(t) \sim \rho V^{3/2} D^{1/2} t^{-1/2}$ (see Section 2.2). Marengo et al. (2011) further suggested that the velocity field in an impacting drop can be approximated by the irrotational flow past a disk of radius $r_0(t)$, where $r_0(t)$ is the radius of the turning line. At the impact point, the velocity potential of the flow past a disk is known as $\phi = -2Vr_0/\pi$ (Batchelor 1967). The pressure can then be calculated using the unsteady Bernoulli's equation,

$$\frac{p}{\rho} + \frac{\partial \phi}{\partial t} + \frac{1}{2}(\nabla \phi)^2 = \frac{1}{2}V^2. \quad 8.$$

The pressure at the stagnant point with $\nabla \phi = 0$ is

$$p(r = 0, t) = \frac{1}{2}\rho V^2 + \frac{2\rho V}{\pi}\frac{dr_0}{dt} = \frac{1}{2}\rho V^2 + \frac{\sqrt{6}}{2\pi}\rho V^{3/2} D^{1/2} t^{-1/2}, \quad 9.$$

where we use $r_0(t) = \sqrt{6DVt}/2$ instead of the radius of a truncated sphere suggested in the original derivation by Marengo et al. (2011).

A similar analogy between drop impact and flow past a radially expanding disk has also been made by Philippi et al. (2016). Based on the analogy, they calculated the self-similar potential flow during early impact near the tip. Their theory provided the analytical solution of the turning line $r_0(t)$ and revealed the singular structure of the pressure distribution over the contact area,

$$p(r, t) = \frac{3\sqrt{2}}{2\pi}\frac{\rho V^2 D}{\sqrt{3VDt - 2r^2}}. \quad 10.$$

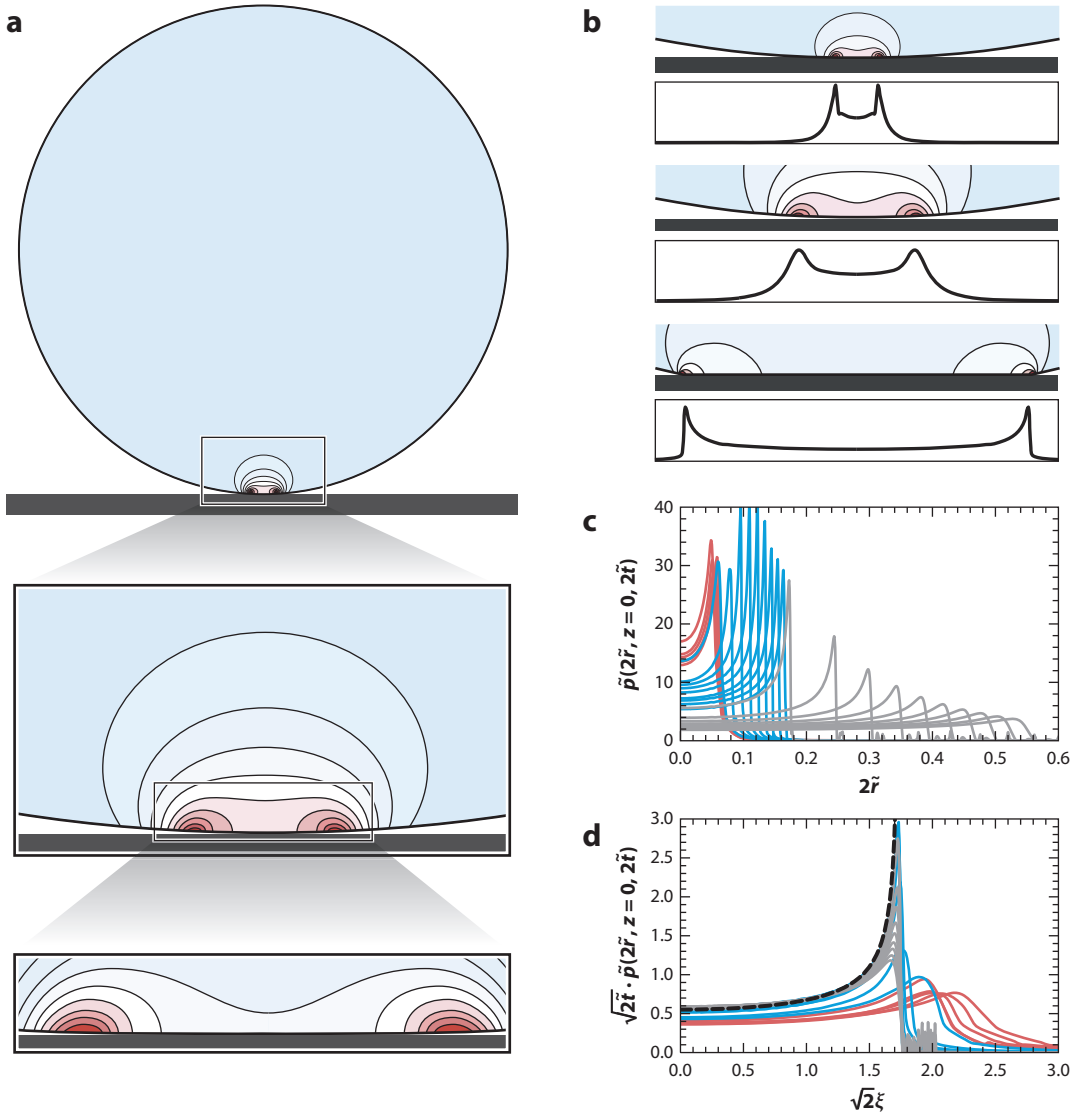

Figure 5

Pressure distribution of drop impact at Reynolds number $Re = 5{,}000$ and Weber number $We = 250$ at early times from numerical simulations. (*a*) Close-up view of the pressure field inside an impacting drop at early times, $\tilde{t} = 2 \times 10^{-4}$. (*b*) Time series showing the development of the pressure field (*top panels*), as well as the pressure on the impacted surface (*bottom panels*). From top to bottom, $\tilde{t} = 5 \times 10^{-5}$, 5×10^{-4}, and 5×10^{-3}. (*c*) Pressure $\tilde{p}$ at the contacted surface at different times. Time increases from red to blue to gray. (*d*) Pressure as a function of the rescaled variable $\xi = \tilde{r}/\sqrt{\tilde{t}}$. The black dashed line is the theoretical prediction (Equation 10). Figure adapted with permission from Philippi et al. (2016).

Equation 10 reduces to Equation 9 at the drop axis $r = 0$, except for a constant dynamic pressure that can be adsorbed by redefining the reference pressure. More importantly, it reveals a finite-time singularity at the turning line $r_0(t)$ away from the impact axis. The prediction quantitatively agrees with volume-of-fluid numerical simulations (**Figure 5**). Particularly, Equation 10 predicts an annular ring of divergent pressure propagating radially with the turning line (**Figure 5*b*,*c***).

Such a noncentral pressure maximum is in sharp contrast to the pressure distribution induced by a steady jet of a liquid impinging on a flat wall, where the pressure maximum is expected at the central stagnation point. For steady flows, we have $\partial\phi/\partial t = 0$ in Equation 8. Since the kinetic term is $(\nabla\phi)^2/2 \geq 0$, the pressure $p = \rho[V^2 - (\nabla\phi)^2]/2$ reaches maximum at the central stagnant point. In contrast, the acceleration term $\partial\phi/\partial t$ dominates drop impact, leading to the counter-intuitive off-axial pressure maximum (Josserand & Zaleski 2003, Philippi et al. 2016). The integration of Equation 10 over the contact area within the turning line gives the impact force in Equation 1.

It is clearly difficult to conduct experimental measurements on the transient pressure distribution underneath millimeter-sized drops with micron spatial resolutions and submillisecond temporal resolutions. Early experiments assessing the damage of solid surfaces induced by high-speed drop impacts with impact velocities >200 m/s showed patterns of ring cracks on the impacted surfaces, indicating the existence of annular pressure peaks (**Figure 6*a***) (Adler 1977, Hackworth 1979). Experiments have also been conducted by shooting cylindrical bullets at high speeds into 2D drops or the side of vertical liquid jets. Pressure was measured by embedded small piezoelectric sensors on the surface of the bullets. An off-axial pressure maximum has been observed, although the temporal variation of the pressure distribution has not been reported (**Figure 6*b***) (Rochester & Brunton 1979, Lesser & Field 1983). Using an array of miniature force sensors based on microelectromechanical systems, Thanh-Vinh and coworkers measured the temporal evolution of pressure distributions under impacting drops of low impact velocities relevant to this review (Thanh-Vinh et al. 2016, Thanh-Vinh & Shimoyama 2019). Nevertheless, the spacing between the force sensors in their experiments was too large to resolve the fine structure of the pressure distribution predicted in Equation 10. More recently, the authors of this review measured the temporal evolution of the stress distributions of drop impact by imaging the deformation of elastic gels underneath impacting drops (Sun et al. 2021). The measurements provided experimental evidence of the noncentral propagating pressure maximum for drop impact (**Figure 6*c***).

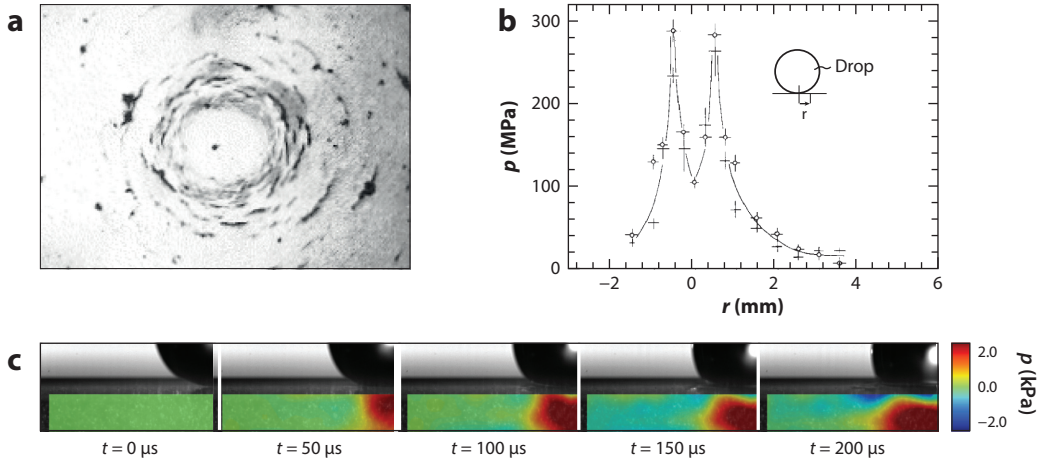

Figure 6

Impact pressure from experiments. (*a*) Ring fracture formed on chemically vapor-deposited zinc sulfide due to the impact of a 2-mm-diameter water drop at an impact velocity of $V = 340$ m/s. The width of the picture is 2.89 mm. Panel *a* adapted with permission from Hackworth (1979). (*b*) Peak pressure p at different positions r under a 2D water drop of diameter 5.0 mm with an impact velocity of $V = 100$ m/s. Panel *b* adapted with permission from Rochester & Brunton (1979). (*c*) Temporal variation of the pressure distribution underneath a 3.5-mm-diameter drop of sodium iodide aqueous solution (60% weight per weight) with a drop impact of $V = 2.97$ m/s. Panel *c* data from Sun et al. (2021).

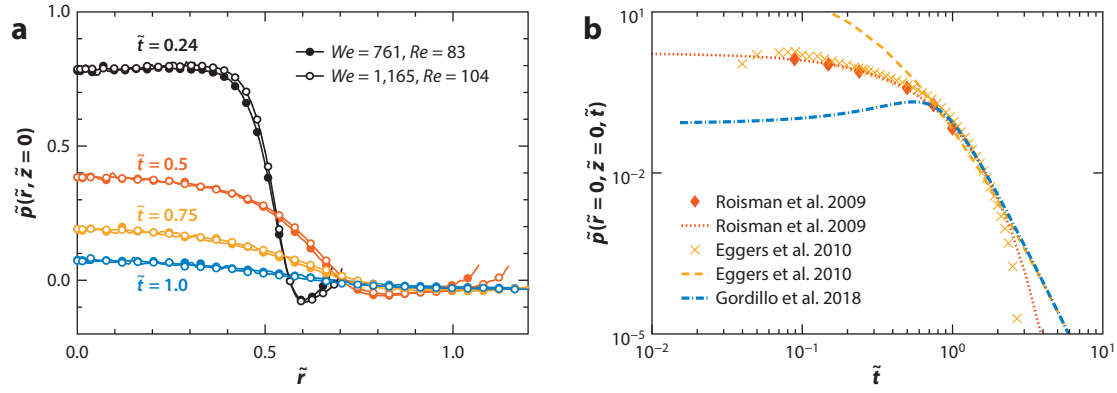

Figure 7

Pressure distribution during drop spreading. (*a*) Numerical results showing the pressure $\tilde{p}$ near the impacted surface as a function of the radial position $\tilde{r}$ at different times $\tilde{t}$. The impacted surface is treated as a symmetric plane with a slip boundary condition. Panel *a* adapted with permission from Roisman et al. (2009). (*b*) Pressure at the impact axis. Symbols are numerical results at high Reynolds number *Re* and Weber number *We* from Roisman et al. (2009) and Eggers et al. (2010). Lines are fittings (Roisman et al. 2009) and theoretical predictions (Eggers et al. 2010, Gordillo et al. 2018).

3.1.2. Late-impact regime. Inertia-driven drop spreading at high *Re* and *We* in the late-impact regime leads to a universal pressure field away from the edge of the spreading lamella. Roisman et al. (2009) numerically solved the universal pressure distribution along the contact surface in the late-impact regime (**Figure 7*a***). They found that the contact pressure at the center of spreading drops can be fitted with an exponentially decaying function, $p(r = 0, t) = 1.7\rho V^2 \exp(-3.1Vt/D)$ (**Figure 7*b***).

The pressure at the impact axis has also been simulated by Eggers et al. (2010) (**Figure 7*b***). They further analytically solved the asymptotic pressure distribution along the contact surface in the limit $t \to \infty$: $p(r, t) = 3\rho h^2(r, t)/(t + t_0)^2$ (see Section 2.3). Here, the free surface of the spreading drop is $h(r, t) = h_{\max}(t)G(\xi)$, with $h_{\max}(t) = h(r = 0, t)$ the maximum drop height at the impact axis. While $h_{\max}(t) = A_1 D^3/[V(t + t_0)]^2$ can be derived from the mass conservation with A_1 as a numerical constant (Roisman et al. 2009), the scaling function $G(\xi \equiv r\sqrt{h_{\max}/V_0})$ is obtained from either experiments (Lagubeau et al. 2012, Lastakowski et al. 2014) or simulations (Eggers et al. 2010). An empirical function has been proposed, $G(x) = 1/(1 + Cx^2)^6$, with $C = 0.625$ from simulations (Eggers et al. 2010) and $C = 0.604$ from experiments (Lastakowski et al. 2014). Thus, an analytical formula for the pressure distribution underneath a spreading drop is reached,

$$p(r,t) = \left[\frac{3\rho A_1^2 D^6}{V^4(t+t_0)^6}\right]\left[\frac{\pi V^2(t+t_0)^2}{\pi V^2(t+t_0)^2 + 6CA_1 r^2}\right]^{12}, \qquad 11.$$

where $A_1 = 0.492$ and $t_0 = 0.429D/V$ are obtained from the experimental profile of spreading drops (Lagubeau et al. 2012), and $A_1 = 0.39$ and $t_0 = 0.25D/V$ are obtained from the numerical profile of spreading drops (Roisman et al. 2009). The calculation by Eggers et al. is valid at the long-time limit when $p \to 0$. Gordillo et al. (2018) further extended the self-similar scaling of drop spreading and provided a fully nonlinear self-similar analytical solution for $h_{\max}(t)$ and $p(r, t)$, valid at finite times in the late-impact regime of inviscid-drop impacts. In the $t \to \infty$ limit, their theory analytically predicts $A_1 = 0.44$ and $t_0 = 0.31D/V$, which are in close agreement with fitted parameters of experiments and simulations. The pressure at the impact axis was also given in a

parametric representation

$$\tilde{p}(\hat{\omega}) = -\frac{1}{8t_2^2}\frac{\hat{\omega}T''(\hat{\omega})}{T^3(\hat{\omega})} \quad \text{and} \quad \tilde{t}(\hat{\omega}) = t_1 + t_2 T(\hat{\omega}), \tag{12.}$$

where $t_2 = \sqrt{2}/3$, $t_1 = -t_2 T(2)$, and $T(x) = 2x^{-1/2}(1 + x^3)^{1/2} - 3(1 + x^3)^{1/3}F_{[-1/3,\,1/6,\,2/3]}[(1 + x^3)^{-1}]$, with $F_{[m,\,n,\,p]}(x)$ a hypergeometric function. Different theoretical predictions are compared in **Figure 7*b***.

We end this section with two remarks. First, Equations 11 and 12 predict $p(t)$ behaves asymptotically following $1/(t + t_0)^6$ at the impact axis, which is different from the exponential decay suggested based on the fitting of numerical results (**Figure 7*b***). Nevertheless, the formulas numerically converge in the regime of inertia-driven spreading for $0.5 < \tilde{t} < 2$. At even longer times toward the end of spreading, the inertia-driven universal pressure profile is invalid due to the action of viscous and capillary forces. Second, since the maximum pressure of spreading drops occurs at the impact axis, the pressure maximum has to shift from the position of the turning line near the edge of impacting drops to the center of the drops during the transition from the early-impact to the late-impact regime (Eggers et al. 2010, Bako et al. 2016). It is still not clear how the shift proceeds theoretically (see the Future Issues section).

3.2. Shear Stress

Next, we consider the shear stress distribution of drop impact, which is more relevant to the erosion induced by drop impact. At high *Re* and *We*, the viscous boundary layer is thin and scales as $\tilde{l}_v \sim \sqrt{\tilde{t}/Re}$. Pressure gradients across this thin viscous boundary layer are small. Hence, to the first order, the pressure distribution is not affected by the viscous boundary layer. Nevertheless, the boundary layer plays the essential role for the shear stress on impacted surfaces. Ignoring the viscous boundary layer would lead to zero shear stress and significantly reduce the erosion capability of impacting drops (Bako et al. 2016).

3.2.1. Early-impact regime. In the early-impact regime, Philippi et al. (2016) hypothesized that the structure of the viscous boundary layer of drop impact is similar to that of the shock wave–induced boundary layer. Here, the turning line of an impacting drop is analogous to a shock front with a growing viscous boundary layer trailing behind. Based on the classic shock wave solution (Mirels 1955), they obtained the velocity profile within the boundary layer and calculated the shear stress distribution along the contact surface,

$$\tau(r,t) = \eta\frac{\partial v_r(r,z=0,t)}{\partial z} = \frac{\sqrt{6}\rho^{1/2}V^{3/2}D^{1/2}\eta^{1/2}}{\pi^{3/2}}\frac{2r}{3VDt - 2r^2}, \tag{13.}$$

where η is the dynamic viscosity of fluid. Similar to the pressure distribution (Equation 10), the shear stress also exhibits a finite-time singularity at the turning line $r_0(t)$. The formula agrees well with numerical simulations away from the singularity (**Figure 8*a***). A small cutoff Δ was found near the turning line, below which the $1/r$ singularity is screened (**Figure 8*b***). By integrating the shear stress over the contact area, they also derived the magnitude of the drag force induced by drop impact in the early-impact regime,

$$F_d(t) = \int_0^{2\pi}\int_0^{r_0-\Delta}\tau(r,t)r\,dr\,d\theta = 5.35\eta^{1/2}\rho^{1/2}V^2D\sqrt{t}, \tag{14.}$$

where $\Delta = 0.02\sqrt{VDt}$ is chosen based on numerical findings at different *Re*.

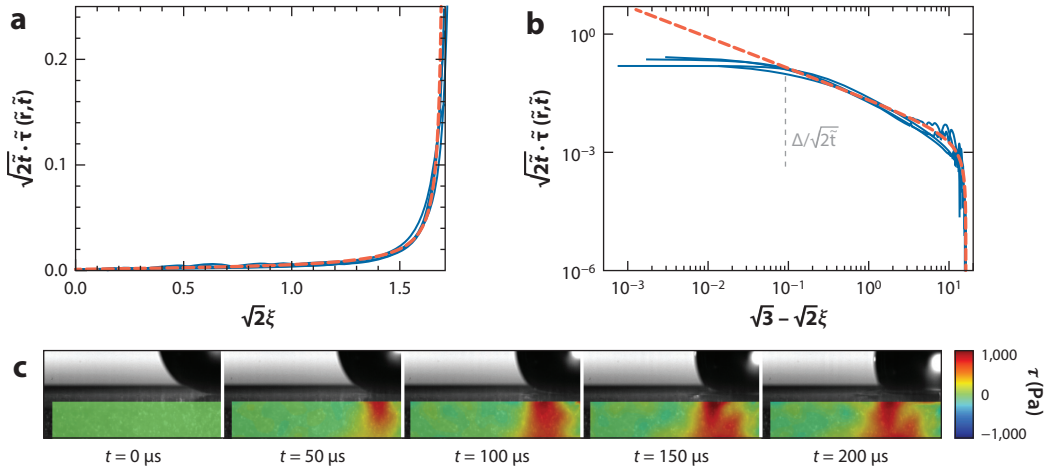

Figure 8

Shear stress distribution in the early-impact regime. (*a*) Shear stress τ from numerical simulations with Reynolds number $Re = 5{,}000$ and Weber number $We = 250$ at different times, represented in the self-similar variables $\xi = \tilde{r}/\sqrt{\tilde{t}}$. The red dashed line is the theoretical prediction (Equation 13). (*b*) Same data represented as a function of the distance from the turning line. A cutoff Δ is indicated, below which the $1/x$ singularity is screened. Panels *a* and *b* adapted with permission from Philippi et al. (2016). (*c*) Experimental shear stress distribution underneath an impacting drop. Impact conditions are the same as those in **Figure 6*c***. Panel *c* data from Sun et al. (2021).

Our recent experiments with elastic gels confirmed the existence of a propagating shear stress maximum (**Figure 8*c***). The position of the maximum shear stress is slightly behind the turning line, following a square-root temporal scaling. The drag force from our latest experiments also quantitatively agrees with Equation 14 after a transient time upon impact.

3.2.2. Late-impact regime. The viscous boundary layer plays a more prominent role in determining the shape of impacting drops in the late-impact regime during drop spreading (Roisman 2009, Eggers et al. 2010, Schroll et al. 2010). The final thickness of the spreading lamellae of viscous drops is set by the thickness of the viscous boundary layer at the time when the growing layer meets with the decreasing surface of the spreading drops.

A simple scaling can be formulated for the shear stress during drop spreading (Bako et al. 2016). As discussed in Section 2.3, inertia-driven drop spreading is governed by a hyperbolic flow with $v_r \sim r/t$. The thickness of the viscous boundary layer grows as $l_v \sim \sqrt{\nu t}$. Thus, the shear stress scales as $\tau(r,t) \sim \eta v_r/l_v \sim \rho\sqrt{\nu} r t^{-3/2}$. More detailed analysis confirmed the scaling with a numerical factor close to one (Roisman 2009, Eggers et al. 2010):

$$\tau(r,t) = 1.0354\sqrt{\nu}\rho r t^{-3/2}. \qquad 15.$$

Equation 15 shows that $\tau(r, t)$ increases linearly with r and reaches a maximum at the edge of the spreading lamella, where a thick rim is formed due to the capillary force and the hyperbolic velocity profile is invalid. After the stress maximum, the shear stress quickly relaxes to zero toward the edge of the rim (Bako et al. 2016). The function form of the shear stress in the rim of spreading drops has not been studied. Differently from the pressure distribution, where the maximum pressure shifts from the edge of an impacting drop to the center of the drop during the transition from the early-impact to the late-impact regime, the maximum shear stress stays near the edge of the impacting drop in the entire impact process. Indeed, due to the axial symmetry of drop impact, the shear stress is necessarily zero at the impact axis.

4. OTHER FACTORS

Studies of the impact force and the stress distributions in an ideal impact situation, where spherical drops impact on smooth solid surfaces, have been inspired and motivated by related problems that include other factors, such as the presence of fluid layers, the effect of air cushioning, and nonspherical impacting drops.

4.1. Fluid Layers

The preexisting fluid layer on impacted surfaces can significantly modify the impact force and stress distributions.

4.1.1. Impact force. Petersson (1995) experimentally studied the drop impact force on a solid surface covered by a water layer using an underwater piezoelectric sensor. Although the exact thickness of the water layer was not measured, Petersson showed that the peak force decreases and the width of the force peak increases with increasing thickness of the water layer. More recently, Yu & Hopkins (2018) used the technique of wavelet deconvolution and studied the temporal evolution of the drop impact force on an elastic plate underneath a water layer of controlled thickness. The force–time curves can be generally divided into two parts in their experiments: the short-time dynamics due to the initial impact and the long-time dynamics associated with the formation of jets, vortex rings, or oscillating bubbles induced by the impacting drops (Yarin 2006). While the force impulse of the initial impact broadens with the thickness of the water layer, consistent with Petersson's experiments, the force at long times is more complicated because of complex flow dynamics in the water layer. Particularly for small drops impacting into deep layers, bubbles are entrained underneath the impact point. The oscillation of these bubbles gives rise to strong force signals at high frequencies above 700 Hz in the frequency domain.

4.1.2. Stress distributions. Early studies by Hartley and coworkers investigated impact-induced shear stress on a solid surface underneath water layers of different thicknesses (Hartley & Alonso 1991, Hartley & Julien 1992). They focused on the short-time dynamics during the expansion of impact craters in the water layer. Based on numerical simulations at intermediate *Re*, they obtained a series of empirical relations for various features of the shear stress distribution, including the maximum shear stress, the position and time of the maximum shear stress, and the spatial distribution of the shear stress. Particularly, they suggested that the maximum shear stress on the solid surface follows

$$\tau_{\max} = 4.17 C_1 \rho V^2 (2h/D + 1)^{-3.16} Re^{-0.55}, \qquad 16.$$

where h is the thickness of the water layer. The prefactor C_1 ranges between 0.91 and 1 and is a weak function of a specific combination of *We* and *Fr*. Equation 16 shows a strong dependence of $\tau_{\max}$ on the thickness of the water layer. Water layers effectively shield the shear stress at the solid surface, a known effect from the study of soil erosion (Mutchler & Young 1975, Bako et al. 2016). The decay of shear stress after the maximum shows a strong dependence on *We* and *Fr*, as gravity and surface tension provide the restoring force for the disturbed water layer. Using hot-film anemometry, Hartley and coworkers further experimentally measured the shear stress of drop impact on the bottom surface of a water flume. A slow horizontal base flow had to be imposed in the flume in order to maintain a constant fluid temperature over the hot-film sensor in their experiments. A qualitative agreement between numerical and experimental results was found.

Thanks to advances in computational power, simulations of the pressure and shear stress of drop impact on water layers can now be extended to high *Re*, which is relevant to raindrop impact.

Bako et al. (2016) showed that the position of the maximum pressure inside the water layer follows the square-root scaling, $r_{max}(t) \sim \sqrt{t}$, similar to that of drop impact on dry surfaces. For shallow water layers of height $h/D < 1/4$, the maximum pressure is $p_{max}(t) \sim 1/\sqrt{t}$, which also agrees with the prediction of Equation 9. For thick layers, the maximum pressure is $p_{max}(t) \sim 1/t$ at intermediate times and transitions to $\sim 1/\sqrt{t}$ at long times. The crossover time between the two scaling behaviors increases with increasing h/D. While $r_{max}(t)$ within water increases with time, the maximum pressure on the solid surface underneath the water layers stays at $r = 0$. Thus, water layers eliminate the annular pressure maximum on the solid surface. Nevertheless, self-similar structures of the pressure field could still be identified, although the scaling parameters vary with h/D. For the maximum shear stress on the solid surface, Bako et al. (2016) found $\tau_{max}/(\rho V^2) \sim (2h/D + 1)^{-2.6}$, which shows a weaker dependence on the thickness of the water layer than that predicted by Equation 16. Self-similar structures of shear stress distributions were observed for shallow ($h/D < 1/3$) and thick ($h/D > 1$) water layers, but not for water layers of intermediate thicknesses.

4.2. Air Cushioning

Since the discovery of the effect of ambient air on the splashing of impacting drops on solid surfaces (Xu et al. 2005), air cushioning in drop impact has attracted great research interests [see Josserand & Thoroddsen (2016) and references therein]. The thin layer of air underneath an impacting drop induces a submicron dimple-like deformation on the bottom of the drop and delays the contact between the drop and the solid surface (**Figure 9*a***) (Thoroddsen et al. 2005, Driscoll & Nagel 2011, Kolinski et al. 2012, Lee et al. 2012). This effect of air cushioning screens the $1/\sqrt{t}$ singularity of the pressure at the impact point predicted by Equations 9 and 10, as well as the water-hammer pressure at the very early moment of impact. Smith et al. (2003) calculated the screened pressure on the impacted surface. Before the drop touches the surface, a maximum gas pressure first builds up at the impact axis. As the impact pressure overcomes the gas pressure, an annular pressure maximum develops at later times along a ring where the distance between the bottom of the deformed drop and the surface is smallest at h_{min}. Similar dynamics have also been

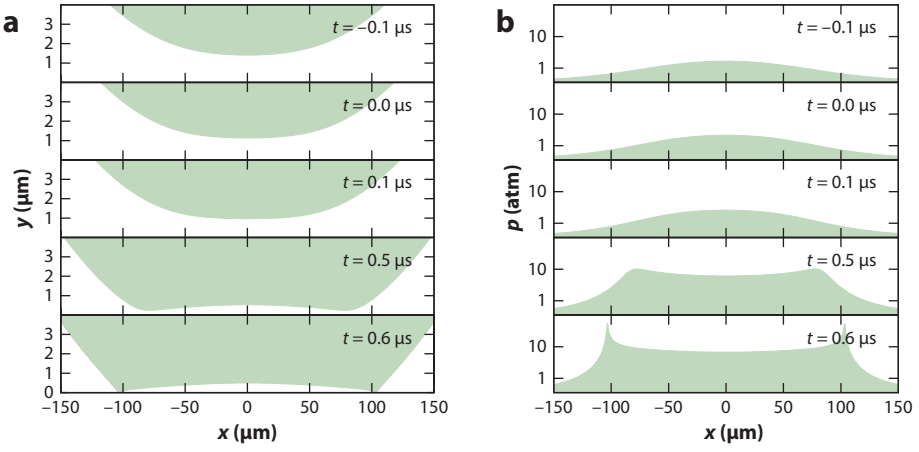

Figure 9

Air cushioning effect. (*a*) Snapshots from simulations showing the deformation of a drop of diameter $D = 3.4$ mm ($\eta_g = 1.8 \times 10^{-5}$ Pa·s, $\rho = 0.78$ g/cm^3) before contacting the impacted surface at an impact velocity of $V = 3.74$ m/s. (*b*) The corresponding gas pressure within the air layer. Figure adapted with permission from Mani et al. (2010).

Stokes number: $St = \eta_a/(\rho VD)$

reported by Mandre and coworkers (**Figure 9*b***) (Mandre et al. 2009, Mani et al. 2010), who further showed that the air underneath the impacting drop can either drain out of the thin layer or be compressed, depending on specific impact parameters and the ambient pressure. The compression dynamics are further divided into two different regimes in their theory: the subcompressible regime at large h_{min} and the supercompressible regime at small h_{min}. In all the cases, the pressure distributions near h_{min} can be described by self-similar solutions.

Coupling the potential flow of the impacting drop with the lubrication flow of the thin incompressible air film, Hendrix et al. (2016) studied the air entrainment induced by drop impact on a deep liquid pool. Their simulations revealed a similar pressure screening effect by air cushioning, where the maximum gas pressure moves from the impact axis to the contact ring between the drop and the pool. Josserand et al. (2016) also discussed the effect of air cushioning in regularizing the pressure singularity at the turning line for drop impacts on a thin liquid film. In the draining regime without air compression, they showed that the pressure inside an air layer of viscosity η_a follows $p \sim \rho V^2 St^{-1/3}$, where the Stokes number St compares the viscous effect of air with drop inertia. The proposed scaling agrees with their simulations. Systematic experiments investigating the effect of air cushioning on the impact force and stress distributions of drop impact have not been conducted so far (see the Future Issues section).

4.3. Nonspherical Drops

Drops under equilibrium form perfectly spherical shapes due to the action of capillary forces. However, drops in nature are often in an out-of-equilibrium state. For instance, drops may oscillate between a prolate and oblate shape due to the initial perturbations (Lamb 1945). The amplitude of the oscillation diminishes over time because of viscous dampening. Likewise, large drops falling at their terminal velocities are deformed due to air drag, leading to nonspherical shapes with flatter bottoms (Clift et al. 1978). The effects of the nonspherical shape on the impact force of liquid drops have been examined in several experiments and simulations.

The first evidence of the shape-dependent impact force was from the early study of Nearing & Bradford (1987), who showed that the peak force oscillates with the release height. They verified the shape origin of the force oscillation by showing that the oscillation amplitude decreased with the fall time. For a millimeter-sized water drop released from a 14-m height, the oscillation amplitude is a few percent of the mean peak force. More recently, Zhang et al. (2019) studied the impact force of ellipsoidal drops of different aspect ratios in simulations. They found that oblate drops have larger peak forces and shorter peak times compared with prolate drops of the same impact momentum. They further showed that the impact force of ellipsoidal drops exhibits the same square-root temporal scaling at early times as the impact force of spherical drops (Equation 1). The higher peak force induced by the impact of oblate drops has been confirmed by recent experiments comparing the temporal evolution of the impact force of oblate, spherical, and prolate drops (Schmid et at. 2021). When nondimensionalized by the nominal diameter $D = (6V_0/\pi)^{1/3}$ defined in terms of the drop volume V_0, the dimensionless peak force of large drops near terminal velocities is larger than $\tilde{F}_{max} = 0.85$ of the universal force curve (Yu & Hopkins 2018). The deviation is attributed to the oblate shape of large drops induced by air drag, which gives rise to the higher peak force.

5. SURFACE EROSION AND GRANULAR IMPACT CRATERING

The pressure and shear stress of drop impact are responsible for the wear and erosion of impacted surfaces, which motivated many of the studies reviewed above. In this last section, we briefly discuss impact-induced surface erosion on granular media as an example illustrating the outcome of

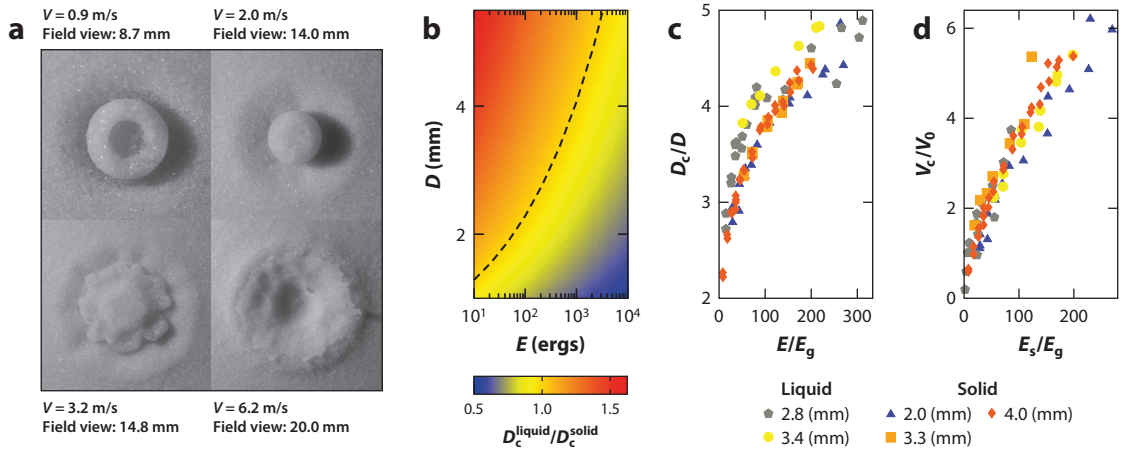

Figure 10

Granular impact cratering by liquid drops. (*a*) Morphology of granular craters induced by the impact of 3.1-mm-diameter water drops. Panel *a* adapted with permission from R. Zhao et al. (2015). (*b*) Ratio D_c^{liquid}/D_c^{solid} of the diameter of granular craters by water drops to that by solid spheres at different projectile sizes D and energies E based on Equations 17 and 18. The dashed line indicates the sizes and energies of projectiles where the ratio is 1. Above the line, liquid drop craters are larger. (*c*) Comparison of the diameter of drop craters and that of solid-sphere craters. $E_g = (\pi/6)\rho_g \phi g D^4$ is the characteristic potential energy, where ϕ is the volume fraction of granular media. (*d*) Excavated crater volume V_c normalized by $V_0 = (\pi/6)D^3$ versus the scaled granular deformation energy E_s/E_g. Panels *c* and *d* adapted with permission from de Jong et al. (2021).

the unique spatiotemporal structure of the stress distributions of impacting drops. Although the erosion of hard solid surfaces by high-speed impacting drops have been investigated (**Figure 6*a***) (Adler 1977, Hackworth 1979), the study of the erosion effect of low-speed drop impact relevant to the current review focuses mainly on deformable granular media. We limit our review on the process of impact cratering by single drops on dry granular media. Other effects such as the ejection of granular particles, the so-called rain splash, and impact on wet granular media can be found in the literature (see Furbish et al. 2007, Long et al. 2014, Zhang et al. 2015, and references therein).

Under the impact of a liquid drop, the surface of a granular medium readily deforms. Granular particles on the surface are pushed away from the impact point by the spreading drop, leading to an impact crater as the final outcome of the impact event (**Figures 1*a*** and **10*a***). Early experiments investigated the scaling of the diameter D_c of liquid drop impact craters on granular media (Katsuragi 2010, Marston et al. 2010, Delon et al. 2011). These experiments suggested that D_c scales with the 1/4 power of We of impacting drops, which yields $D_c \sim E^{1/4}$, where E is the impact energy of the drops. Nevertheless, later studies extending over a larger range of impact energies showed the scaling exponent is less than 1/4 due to the internal dissipation associated with drop deformation (Nefzaoui & Skurtys 2012, R. Zhao et al. 2015). R. Zhao et al. (2015) proposed a scaling relation for the diameter of impact craters:

$$D_c = 1.74\,(\rho g)^{-1/6} D^{1/3} E^{1/6}. \qquad 17.$$

The van der Meer group has conducted a series of experiments investigating both the dynamics of impacting drops on granular surfaces and the shape of resulting impact craters (S.-C. Zhao et al. 2015, 2017, 2019; de Jong et al. 2017, 2021). They showed that the energy transferred from impacting drops to granular media can be expressed as $E_s = Z_c^* E/(D/2 + Z_c^*)$, where Z_c^* is the maximum crater depth. A scaling of $D_c/D \sim E_s^{0.16}$ has been found.

As a comparison, the scaling of the size of impact craters by solid spheres has also been obtained from experiments (Uehara et al. 2003),

$$D_c = 0.92\left[\frac{\rho}{\rho_g \mu^2}\right]^{1/4} D^{3/4} H^{1/4} = 1.08\left[\frac{1}{\rho_g g \mu^2}\right]^{1/4} E^{1/4}, \quad 18.$$

where H is the fall height of solid spheres, ρ_g is the density of granular particles, and μ is the grain friction coefficient. Note that the impact energy is $E = (\pi/6)D^3 \rho g H$.

The different scaling behaviors of the two impact processes arise due to the distinctive dynamic features of their stress distributions. Equation 18 shows that, when plotted against the impact energy, the size of craters from solid-sphere impact is independent of the size of spheres. As the positions of the maximum impact pressure and the maximum shear stress of solid-sphere impact are stationary, concentrating near the impact point, the process of solid-sphere impact can be viewed as the deposit of a point-source energy on the granular surface, similar to explosion cratering (Gao et al. 2017, Liu et al. 2020). As a result, the crater size is independent of the size or even the shape of the impacting sphere when the impact energy is sufficiently high (Pacheco-Vazquez 2019). In contrast, the maximum pressure and shear stress of drop impact expand radially in an impact event (**Figures 6*c*** and **8*c***). Since the spreading of impacting drops is a strong function of the size of the drops, the resulting granular craters exhibit a clear size dependence (Equation 17).

As a consequence of this size dependence, the diameter of impact craters by large drops at low impact energies is larger than that of solid-sphere impact craters at the same impact energy, even though the average impact force and pressure of drop impact are significantly smaller than those of solid-sphere impact (**Figure 10*b***). More recent experiments by de Jong et al. (2021) directly compared the sizes of granular craters by drop impact and those by solid-sphere impact. Their study indeed showed larger impact craters by water drops at relatively low impact energies (**Figure 10*c***). In addition, they showed that the drop impact craters are shallower than those from solid spheres. More interestingly, they found that the excavated crater volume is the same for both drop and solid-sphere impact when plotting against the granular deformation energy E_s (**Figure 10*d***).

FUTURE ISSUES

1. While the self-similar dynamics in both the early-impact and the late-impact regimes have been elucidated thanks to recent theoretical progress, an understanding of the transition between the two regimes at intermediate times is still out of reach. As a result, a first-principle description of the dynamics of impact force and stress distributions over the entire time domain of drop impact has not yet been achieved. As the maximum impact force occurs in this transition regime, a theoretical understanding of the regime will provide a quantitative prediction of the peak impact force, which is crucial for many impact-related processes.
2. Quantitative measurements of the stress distributions underneath impacting drops are highly demanded and are important not only for verifying the key assumptions of theories and simulations but also for understanding the dynamics of drop impact in situations that are hard to simulate at present (e.g., drop impact on granular media). For such challenging measurements, new experimental techniques are likely needed.
3. Although extensive research has been conducted in probing the kinematics of drop impact across a large control parameter space, the study of the impact force and stress

distributions under different impact conditions requires further efforts. The effects of important parameters on the dynamical variables of drop impact, including the texture of impacted surfaces, the impact angle of impinging drops, and the pressure of ambient gases, have not been systematically investigated. Understanding the influence of these parameters will open the door for manipulating and exploiting the impact force and stress distributions of drop impact in engineering applications.

4. Experiments on the impact force of low–Reynolds number drops without viscoelasticity are needed to detect the higher-order effect of viscosity on the peak force and time (**Figure 4**). It would also be interesting to investigate the impact force and stress distributions of viscoelastic drops and explore the transition between drop impact and solid sphere impact from the perspective of impact dynamics and materials science.
5. A vast knowledge gap still exists between our fundamental understanding of the impact force and stress distributions and the outcome of drop impact events. For example, it is far from clear how the dynamics of impact force and stress distributions lead to the unusual scaling of drop impact granular craters (Equation 17) and how to use the basic understanding presented in this review to predict the degree of soil erosion induced by raindrop impact.

DISCLOSURE STATEMENT

The authors are not aware of any biases that might be perceived as affecting the objectivity of this review.

ACKNOWLEDGMENTS

We are grateful to all coworkers, collaborators, and colleagues who made significant contributions to enrich our understanding of the dynamics of drop impact. We acknowledge the US National Science Foundation awards DMR-1452180, CBET-2017071, and CBET-2002817 and the American Chemical Society Petroleum Research Fund 60668-ND9 for financially supporting our research over the years. L.G. acknowledges the financial support of the grant CONICYT FONDECYT 11170700.

LITERATURE CITED

Adler WF. 1977. Liquid drop collisions on deformable media. *J. Mater. Sci.* 12:1253–71

Bako AN, Darboux F, James F, Josserand C, Lucas C. 2016. Pressure and shear stress caused by raindrop impact at the soil surface: scaling laws depending on the water depth. *Earth Surf. Process. Landf.* 41:1199–210

Barenblatt GI. 1996. *Scaling, Self-similarity, and Intermediate Asymptotics*. Cambridge, UK: Cambridge Univ. Press

Batchelor GK. 1967. *An Introduction to Fluid Dynamics*. Cambridge, UK: Cambridge Univ. Press

Bennett T, Poulikakos D. 1993. Splat-quench solidification: estimating the maximum spreading of a droplet impacting a solid surface. *J. Mater. Sci.* 28:963–70

Bird JC, Dhiman R, Kwon HM, Varanasi KK. 2013. Reducing the contact time of a bouncing drop. *Nature* 503:385–88

Bourouiba L. 2021. The fluid dynamics of disease transmission. *Annu. Rev. Fluid Mech.* 53:473–508

Chen H, Zhang X, Garcia BD, Georgoulas A, Deflorin M, et al. 2019. Drop impact onto a cantilever beam: behavior of the lamella and force measurement. *Interfacial Phenom. Heat Transf.* 7:85–96

Clanet C, Beguin C, Richard D, Quéré D. 2004. Maximal deformation of an impacting drop. *J. Fluid Mech.* 517:199–208

Clift R, Grace JR, Weber ME. 1978. *Bubbles, Drops, and Particles*. New York: Dover

de Jong R, Zhao S-C, Garcia-Gonzalez D, Verduijn G, van der Meer D. 2021. Impact cratering in sand: comparing solid and liquid intruders. *Soft Matter* 17:120–25

de Jong R, Zhao S-C, van der Meer D. 2017. Crater formation during raindrop impact on sand. *Phys. Rev. E* 95:042901

Delon G, Terwagne D, Dorbolo S, Vandewalle N, Caps H. 2011. Impact of liquid droplets on granular media. *Phys. Rev. E* 84:046320

Dickerson AK, Shankles PG, Madhavan NM, Hu DL. 2012. Mosquitoes survive raindrop collisions by virtue of their low mass. *PNAS* 109:9822–27

Driscoll MM, Nagel SR. 2011. Ultrafast interference imaging of air in splashing dynamics. *Phys. Rev. Lett.* 107:154502

Eggers J. 1997. Nonlinear dynamics and breakup of free-surface flows. *Rev. Mod. Phys.* 69:865–929

Eggers J, Fontelos MA. 2015. *Singularities: Formation, Structure, and Propagation*. Cambridge, UK: Cambridge Univ. Press.

Eggers J, Fontelos MA, Josserand C, Zaleski S. 2010. Drop dynamics after impact on a solid wall: theory and simulations. *Phys. Fluids* 22:062101

Ellison WD. 1945. Some effects of raindrops and surface-flow on soil erosion and infiltration. *Eos* 26:415–29

Fedorchenko AI, Wang AB, Wang YH. 2005. Effect of capillary and viscous forces on spreading of a liquid drop impinging on a solid surface. *Phys. Fluids* 17:093104

Field JE, Camus JJ, Tinguely M, Obreschkow D, Farhat M. 2012. Cavitation in impacted drops and jets and the effect on erosion damage thresholds. *Wear* 290:154–60

Furbish DJ, Hamner KK, Schmeeckle M, Borosund MN, Mudd SM. 2007. Rain splash of dry sand revealed by high-speed imaging and sticky paper splash targets. *J. Geophys. Res.* 112:F01001

Gao M, Liu X, Vanin LP, Sun T-P, Cheng X, Gordillo L. 2017. Dynamics and scaling of explosion cratering in granular media. *AIChE J.* 64:2972–81

Gart S, Mates JE, Megaridis CM, Jung S. 2015. Droplet impacting a cantilever: a leaf-raindrop system. *Phys. Rev. Appl.* 3:044019

Ghadiri H, Payne D. 1977. Raindrop impact stress ad the breakdown of soil crumbs. *J. Soil Sci.* 28:247–58

Gordillo JM, Riboux G, Quintero ES. 2019. A theory on the spreading of impacting droplets. *J. Fluid Mech.* 866:298–315

Gordillo L, Sun TP, Cheng X. 2018. Dynamics of drop impact on solid surfaces: evolution of impact force and self-similar spreading. *J. Fluid Mech.* 840:190–214

Grinspan AS, Gnanamoorthy R. 2010. Impact force of low velocity liquid droplets measured using piezoelectric PVDF film. *Colloids Surfaces A* 356:162–68

Hackworth JV. 1979. A mechanistic investigation of the rain erosion of infrared transmitting materials at velocities to Mach 2. In *Proceedings of 5th International Conference on Erosion by Liquid and Solid Impact*, ed. JE Field, Pap. 10. Cambridge, UK: Cavendish Lab.

Hancox NL, Brunton JH. 1966. Erosion of solids by repeated impact of liquid drops. *Philos. Trans. R. Soc. A* 260:121–39

Hartley DM, Alonso CV. 1991. Numerical study of the maximum boundary shear stress induced by raindrop impact. *Water Resour. Res.* 27:1819–26

Hartley DM, Julien PY. 1992. Boundary shear stress induced by raindrop impact. *J. Hydraul. Res.* 30:341–59

Hendrix MHW, Bouwhuis W, van der Meer D, Lohse D, Snoeijer JH. 2016. Universal mechanism for air entrainment during liquid impact. *J. Fluid Mech.* 789:708–25

Howland CJ, Antkowiak A, Castrejon-Pita JR, Howison SD, Oliver JM, et al. 2016. It's harder to splash on soft solids. *Phys. Rev. Lett.* 117:184502

Imeson AC, Vis R, de Water E. 1981. The measurement of water-drop impact forces with a piezo-electric transducer. *Catena* 8:83–96

Josserand C, Ray P, Zaleski S. 2016. Droplet impact on a thin liquid film: anatomy of the splash. *J. Fluid Mech.* 802:775–805

Josserand C, Thoroddsen ST. 2016. Drop impact on a solid surface. *Annu. Rev. Fluid Mech.* 48:365–91
Josserand C, Zaleski S. 2003. Droplet splashing on a thin liquid film. *Phys. Fluids* 15:1650–57
Joung YS, Buie CR. 2015. Aerosol generation by raindrop impact on soil. *Nat. Commun.* 6:6083
Katsuragi H. 2010. Morphology scaling of drop impact onto a granular layer. *Phys. Rev. Lett.* 104:218001
Kim S, Wu Z, Esmaili E, Dombroskie JJ, Jung S. 2020. How a raindrop gets shattered on biological surfaces. *PNAS* 117:13901–7
Kolinski JM, Rubinstein SM, Mandre S, Brenner MP, Weitz DA, Mahadevan L. 2012. Skating on a film of air: drops impacting on a surface. *Phys. Rev. Lett.* 108:074503
Kondo T, Ando K. 2019. Simulation of high-speed droplet impact against a dry/wet rigid wall for understanding the mechanism of liquid jet cleaning. *Phys. Fluids* 31:013303
Laan N, de Bruin KG, Bartolo D, Josserand C, Bonn D. 2014. Maximum diameter of impacting liquid droplets. *Phys. Rev. Appl.* 2:044018
Lagubeau G, Fontelos MA, Josserand C, Maurel A, Pagneux V, Petitjeans P. 2012. Spreading dynamics of drop impacts. *J. Fluids Mech.* 713:50–60
Lamb H. 1945. *Hydrodynamics*. New York: Dover
Lastakowski H, Boyer F, Biance AL, Pirat C, Ybert C. 2014. Bridging local to global dynamics of drop impact onto solid substrates. *J. Fluids Mech.* 747:103–18
Laws JO. 1940. Recent studies in raindrops and erosion. *Agric. Eng.* 21:431–33
Lee JS, Weon BM, Je JH, Fezzaa K. 2012. How does an air film evolve into a bubble during drop impact? *Phys. Rev. Lett.* 109:204501
Lesser MB, Field JE. 1983. The impact of compressible liquids. *Annu. Rev. Fluid Mech.* 15:97–122
Li J, Zhang B, Guo P, Lv Q. 2014. Impact force of a low speed water droplet colliding on a solid surface. *J. Appl. Phys.* 116:214903
Liu T, Cao B, Liu X, Sun T-P, Cheng X. 2020. Explosion cratering in 3D granular media. *Soft Matter* 16:1323–32
Long EJ, Hargrave GK, Cooper JR, Kitchener BGB, Parsons AJ, et al. 2014. Experimental investigation into the impact of a liquid droplet onto a granular bed using three-dimensional, time-resolved, particle tracking. *Phys. Rev. E* 89:032201
Mandre S, Mani M, Brenner MP. 2009. Precursors to splashing of liquid droplets on a solid surface. *Phys. Rev. Lett.* 102:134502
Mangili S, Antonini C, Marengo M, Amirfazli A. 2012. Understanding the drop impact phenomenon on soft PDMS substrates. *Soft Matter* 8:10045–54
Mani M, Mandre S, Brenner MP. 2010. Events before droplet splashing on a solid surface. *J. Fluid Mech.* 647:163–85
Marengo M, Antonini C, Roisman IV, Tropea C. 2011. Drop collisions with simple and complex surfaces. *Curr. Opin. Colloid Interface Sci.* 16:292–302
Marston JO, Thoroddsen ST, Ng WK, Tan RBH. 2010. Experimental study of liquid drop impact onto a powder surface. *Powder Technol.* 203:223–36
Mirels H. 1955. *Laminar boundary layer behind shock advancing into stationary fluid*. Tech. Note 3401, Natl. Adv. Comm. Aeronaut., Washington, DC
Mitchell BR, Bate T, Klewicki J, Korkolis Y, Kinsey B. 2017. Experimental investigation of droplet impact on metal surfaces in reduced ambient pressure. *Proc. Manuf.* 10:730–36
Mitchell BR, Klewicki JC, Korkolis YP, Kinsey BL. 2019a. Normal impact force of Rayleigh jets. *Phys. Rev. Fluids* 4:113603
Mitchell BR, Klewicki JC, Korkolis YP, Kinsey BL. 2019b. The transient force profile of low-speed droplet impact: measurements and model. *J. Fluid Mech.* 867:300–22
Mitchell BR, Nassiri A, Locke M, Klewicki J, Korkolis Y, Kinsey B. 2016. Experimental and numerical framework for study of low velocity water droplet impact dynamics. In *Proceedings of ASME 2016: 11th International Manufacturing Science and Engineering Conference*, Pap. V001T002A047. New York: Am. Soc. Mech. Eng.
Mundo C, Sommerfeld M, Tropea C. 1995. Droplet-wall collisions: experimental studies of the deformation and breakup process. *Int. J. Multiph. Flow* 21:151–73

Mutchler CK, Young RA. 1975. Soil detachment by raindrops. In *Present Prospective Technology for Predicting Sediment Yields and Sources*, pp. 114–17. Washington, DC: US Dep. Agric.
Nearing MA, Bradford JM. 1987. Relationships between waterdrop properties and forces of impact. *Soil Sci. Soc. Am. J.* 51:425–30
Nearing MA, Bradford JM, Holtz RD. 1986. Measurement of force versus time relations for waterdrop impact. *Soil Sci. Soc. Am. J.* 50:1532–36
Nefzaoui E, Skurtys O. 2012. Impact of a liquid drop on a granular medium: inertia, viscosity and surface tension effects on the drop deformation. *Exp. Therm. Fluid Sci.* 41:43–50
Obreschkow D, Dorsaz N, Kobel P, de Bosset A, Tinguely M, et al. 2011. Confined shocks inside isolated liquid volumes: a new path of erosion? *Phys. Fluids* 23:101702
Pacheco-Vazquez F. 2019. Ray systems and craters generated by the impact of nonspherical projectiles. *Phys. Rev. Lett.* 122:164501
Palmer RS. 1965. Water drop impact forces. *Trans. Am. Soc. Agric. Eng.* 8:69–71
Pepper RE, Courbin L, Stone HA. 2008. Splashing on elastic membranes: the importance of early-time dynamics. *Phys. Fluids* 20:082103
Petersson BAT. 1995. The liquid drop impact as a source of sound and vibration. *Build. Acoust.* 2:585–624
Philippi J, Lagree PY, Antkowiak A. 2016. Drop impact on a solid surface: short-time self-similarity. *J. Fluid Mech.* 795:96–135
Planchon O, Mouche E. 2010. A physical model for the action of raindrop erosion on soil microtopography. *Soil Sci. Soc. Am. J.* 74:1092–103
Popinet S. 2009. An accurate adaptive solver for surface-tension-driven interfacial flows. *J. Comput. Phys.* 228:5838–66
Prosperetti S, Oguz HN. 1993. The impact of drops on liquid surfaces and the underwater noise of rain. *Annu. Rev. Fluid Mech.* 25:577–602
Rein M. 1993. Phenomena of liquid drop impact on solid and liquid surfaces. *Fluid Dyn. Res.* 12:61–93
Riboux G, Gordillo JM. 2014. Experiments of drops impacting a smooth solid surface: a model of the critical impact speed for drop splashing. *Phys. Rev. Lett.* 113:024507
Riboux G, Gordillo JM. 2017. Boundary-layer effects in droplet splashing. *Phys. Rev. E* 96:013105
Richard D, Clanet C, Quéré D. 2002. Contact time of a bouncing drop. *Nature* 417:811
Rioboo R, Marengo M, Tropea C. 2002. Time evolution of liquid drop impact onto solid, dry surfaces. *Exp. Fluids* 33:112–24
Rochester MC, Brunton JH. 1979. Pressure distribution during drop impact. In *Proceedings of the 5th International Conference on Erosion by Liquid and Solid Impact*, ed. JE Field, Pap. 6. Cambridge, UK: Cavendish Lab.
Roisman IV. 2009. Inertia dominated drop collisions. II. An analytical solution of the Navier–Stokes equations for a spreading viscous film. *Phys. Fluids* 21:052104
Roisman IV, Berberovic E, Tropea C. 2009. Inertia dominated drop collisions. I. On the universal flow in the lamella. *Phys. Fluids* 21:052103
Scardovelli R, Zaleski S. 1999. Direct numerical simulation of free-surface and interfacial flow. *Annu. Rev. Fluid Mech.* 31:567–603
Schlichting H, Gersten K. 2000. *Boundary-Layer Theory*. Berlin: Springer. 8th ed.
Schmid G, Kingan MJ, Panton L, Willmott GR, Yang Y, et al. 2021. On the measurement and prediction of rainfall noise. *Appl. Acoust.* 171:107636
Schroll RD, Josserand C, Zaleski S, Zhang WW. 2010. Impact of a viscous liquid drop. *Phys. Rev. Lett.* 104:034504
Smith FT, Li L, Wu GX. 2003. Air cushioning with a lubrication/inviscid balance. *J. Fluid Mech.* 482:291–318
Soto D, De Larivière AB, Boutillon X, Clanet C, Quéré D. 2014. The force of impacting rain. *Soft Matter* 10:4929–34
Sun T-P, Alvarez-Novoa F, Andrade K, Gutierrez P, Gordillo L, Cheng X. 2021. Erosion by dripping drops: the stress distribution and surface shock wave of drop impact. arXiv:2108.09398 [physics.flu-dyn]
Tatekura Y, Watanabe M, Kobayashi K, Sanada T. 2018. Pressure generated at the instant of impact between a liquid droplet and solid surface. *R. Soc. Open Sci.* 5:181101

Terry JP. 1998. A rainsplash component analysis to define mechanisms of soil detachment and transportation. *Aust. J. Soil Res.* 36:525–42

Thanh-Vinh N, Matsumoto K, Shimoyama I. 2016. Pressure distribution on the contact area during the impact of a droplet on a texture surface. In *Proceedings of the 2016 IEEE 29th International Conference on Micro Electro Mechanical Systems (MEMS)*, pp. 177–80. New York: IEEE

Thanh-Vinh N, Shimoyama I. 2019. Maximum pressure caused by droplet impact is dependent on the droplet size. In *Proceedings of the 2019 20th International Conference on Solid-State Sensors, Actuators and Microsystems and Eurosensors XXXIII*, pp. 813–16. New York: IEEE

Thoroddsen ST, Etoh TG, Takehara K, Ootsuka N, Hatsuki Y. 2005. The air bubble entrapped under a drop impacting on a solid surface. *J. Fluid Mech.* 545:203–12

Uehara JS, Ambroso MA, Ojha RP, Durian DJ. 2003. Low-speed impact craters in loose granular media. *Phys. Rev. Lett.* 90:194301

Ukiwe C, Kwok DY. 2005. On the maximal spreading diameter of impacting droplets on well-prepared solid surfaces. *Langmuir* 21:666–73

Visser CW, Frommhold PE, Wildeman S, Mettin R, Lohse D, Sun C. 2015. Dynamics of high-speed micro-drop impact: numerical simulations and experiments at frame-to-frame times below 100 ns. *Soft Matter* 11:1708–22

Wagner H. 1932. Über Stoß- und Gleitvorgänge an der Oberfläche von Flüssigkeiten. *Z. Angew. Math. Mech.* 12:193–215

Wijshoff H. 2018. Drop dynamics in the inkjet printing process. *Curr. Opin. Colloid Interface Sci.* 36:20–27

Wildeman S, Visser CW, Sun C, Lohse D. 2016. On the spreading of impacting drops. *J. Fluid Mech.* 805:636–55

Worthington AM. 1876. On the forms assumed by drops of liquids falling vertically on a horizontal plate. *Proc. R. Soc.* 25:261–72

Xu L, Zhang WW, Nagel SR. 2005. Drop splashing on a dry smooth surface. *Phys. Rev. Lett.* 94:184505

Yarin AL. 2006. Drop impact dynamics: splashing, spreading, receding, bouncing. . . . *Annu. Rev. Fluid Mech.* 38:159–92

Yarin AL, Roisman IV, Tropea C. 2017. *Collision Phenomena in Liquids and Solids*. Cambridge, UK: Cambridge Univ. Press

Yarin AL, Weiss DA. 1995. Impact of drops on solid surfaces: self-similar capillary waves, and splashing as a new type of kinematic discontinuity. *J. Fluid Mech.* 283:141–73

Yu Y, Hopkins C. 2018. Experimental determination of forces applied by liquid water drops at high drop velocities impacting a glass plate with and without a shallow water layer using wavelet deconvolution. *Exp. Fluids* 59:84

Zhang B, Li J, Guo P, Lv Q. 2017. Experimental studies on the effect of Reynolds and Weber numbers on the impact forces of low-speed droplets colliding with a solid surface. *Exp. Fluids* 58:125

Zhang Q, Gao M, Zhao R, Cheng X. 2015. Scaling of liquid-drop impact craters in wet granular media. *Phys. Rev. E* 92:042205

Zhang R, Zhang B, Lv Q, Li J, Guo P. 2019. Effects of droplet shape on impact force of low-speed droplets colliding with solid surface. *Exp. Fluids* 60:64

Zhao R, Zhang Q, Tjugito H, Cheng X. 2015. Granular impact cratering by liquid drops: understanding raindrop imprints through an analogy to asteroid strikes. *PNAS* 112:342–47

Zhao S-C, de Jong R, van der Meer D. 2015. Raindrop impact on sand: a dynamic explanation of crater morphologies. *Soft Matter* 11:6562–68

Zhao S-C, de Jong R, van der Meer D. 2017. Liquid-grain mixing suppresses droplet spreading and splashing during impact. *Phys. Rev. Lett.* 118:054502

Zhao S-C, de Jong R, van der Meer D. 2019. Formation of a hidden cavity below droplets impacting on a granular substrate. *J. Fluid Mech.* 880:59–72

Zhou Q, Li N, Chen X, Xu T, Hui S, Zhang D. 2008. Liquid drop impact on solid surface with application to water drop erosion on turbine blades, part II: axisymmetric solution and erosion analysis. *Int. J. Mech. Sci.* 50:1543–58